



|                  |  |
|------------------|--|
| Title            | Tortuosity of Internal Pore Space in Variously Structured Platelet Particles   |
| Author(s)        | Ishiyama, Kyoka; Yamamoto, Keita; Harada, Shusaku; Yagi, Tsubasa   |
| Citation         | Transport in porous media, 148(3), 535-557<br><a href="https://doi.org/10.1007/s11242-023-01958-w">https://doi.org/10.1007/s11242-023-01958-w</a>  |
| Issue Date       | 2023-07  |
| Doc URL          | <a href="http://hdl.handle.net/2115/92429">http://hdl.handle.net/2115/92429</a>  |
| Rights           | This version of the article has been accepted for publication, after peer review (when applicable) and is subject to Springer Nature 's AM terms of use, but is not the Version of Record and does not reflect post-acceptance improvements, or any corrections. The Version of Record is available online at: <a href="http://dx.doi.org/10.1007/s11242-023-01958-w">http://dx.doi.org/10.1007/s11242-023-01958-w</a> |
| Type             | article (author version)   |
| File Information | kyoka_final.pdf  |



[Instructions for use](#)

# **Tortuosity in Various-Structured Platelet Particles**

Kyoka Ishiyama<sup>†</sup>, Keita Yamamoto<sup>†</sup>, Shusaku Harada<sup>†\*</sup>, Tsubasa Yagi<sup>‡</sup>

<sup>†</sup> Division of Sustainable Resources Engineering, Faculty of Engineering, Hokkaido University,  
N13-W8, Sapporo, Hokkaido, 060-8628, Japan

<sup>‡</sup> Radioactive Waste Management Funding and Research Center, 6-4, Akashicho, Chuo-ku, Tokyo,  
104-0044, Japan

\* Corresponding author: Shusaku Harada  
Phone/Fax: + (81)-11-7066310  
E-mail address: harada@eng.hokudai.ac.jp

## ABSTRACT

1 Numerical investigations of pore characteristics in platelet particles with various macroscopic  
2 structures were performed for fundamental understanding of transport properties in clay layers  
3 composed of montmorillonite particles. The effect of macroscopic structures of particles on the  
4 geometric characteristics of pore networks were examined, particularly focusing on the tortuosity  
5 which represents the sinuosity of voids. Monte Carlo simulations of platelet particles under various  
6 initial configurations were performed to obtain metastable structures with internal differences. A  
7 random walk analysis was performed in extracted macropores of platelet structures. The tortuosity of  
8 pore network in variously-structured platelet particles was evaluated from the results of the random  
9 walk analysis. The numerical results showed that the macrostructures of particles form complicated  
10 pore networks, which significantly influence the tortuosity. The “diffusional” tortuosity obtained from  
11 the random walk analyses was compared with the existing “geometrical” tortuosity model. It was  
12 found that configurational characteristics of platelets, such as size and orientation angle of particle  
13 clusters, was vital to estimate the tortuosity. The obtained tortuosity was also compared with the  
14 experimental results of the diffusion coefficient in clay layers obtained from previous studies. The  
15 results suggested that a complicated density dependence of diffusivity in clay arises from the diversity  
16 of macroscopic particle structures.

17  
18 **Key words:** tortuosity, platelet particles, macroscopic structures, diffusivity

19

## 20 **1. Introduction**

21 Transport phenomena in porous media is important for many processes in various engineering  
22 fields, such as dispersion process of contamination in soil (Patil and Chore, 2014), engineered barrier  
23 systems of repositories in TRU (Trans-Uranic) waste disposal process (Åkesson, et al., 2010) and so  
24 on. Many previous studies have shown that such transport properties are not simply dependent on  
25 porosity alone, but are affected by various geometric characteristics of pores. For example, the fluid  
26 permeability in porous media has been modeled as functions of the porosity, the specific surface area  
27 and the tortuosity (Carman, 1937). In some cases, the diffusivity has been expressed by the tortuosity  
28 and the constrictivity of pores (Holzer, et al., 2013, Keller, et al., 2015). These pore characteristics  
29 vary significantly depending on the structure of media, for example, the particle size distribution or  
30 packing structure in case of particulate beds.

31 Among the pore characteristics listed above, this study focuses on tortuosity, a crucial parameter  
32 for quantifying pore sinuosity and complexity. As will be discussed later, the tortuosity in porous  
33 media is variously defined in different fields, such as “geometrical” tortuosity, “diffusional” tortuosity,  
34 and so on (Clennell, 1997). There have been various discussions on the validity of existing models  
35 and the compatibility of different definitions of tortuosity (Ghanbarian et al. 2013), and in recent  
36 years, there have been attempts to relate one definition of tortuosity to another (Fu et al. 2021).

37 In porous media composed of solid particles, the particle shape also influences macropore  
38 characteristics including the tortuosity. For example, spherical particle layers have little variation in  
39 pore sinuosity. For this reason, the tortuosity has been modeled as a simple function of porosity (or  
40 apparent density) alone (Millington, 1959; Weissberg, 1963; Boudreau, 1996; Koponen et al., 1996;  
41 Ahmadi et al., 2011). However, layers of anisotropic particles such as platelets and rods, contain  
42 highly complex packing configurations, and consequently internal pore characteristics are also  
43 complicated. Therefore, the tortuosity is not determined by the porosity alone. Accordingly, it is  
44 crucial to account for macroscopic structural properties such as clustering features, when estimating  
45 the tortuosity in anisotropic particle layers. For example, Daigle and Dugan (2011) established the

46 tortuosity model in a cylinder-shaped particle bed, which assumed assemblies of platelet clusters, and  
47 showed that the tortuosity greatly depends on the size and the orientation angle of clusters. Although  
48 the validity of their model has not been fully verified, it illustrates the importance of particle  
49 macrostructures for predicting the tortuosity.

50 Tortuosity in platelet structures is closely related to mass transfer in clay layers, which is important  
51 in TRU waste disposal processes as stated above. Clay particles are well-known to typically exhibit  
52 thin sheet-like shapes, and therefore they are often modeled as platelets in the structural analyses  
53 (Dijkstra et al., 1997). Furthermore, as mentioned above, the tortuosity is related to the diffusivity in  
54 the media, so that evaluating tortuosity in platelet structures aids in understanding the diffusivity in  
55 clay layers. For example, Keller et al. (2011) discussed the diffusion anisotropy in clay layers by  
56 examining the anisotropy of the tortuosity. They constructed a three-dimensional network of flow-  
57 contributing voids in clay layers and quantified the vertical and horizontal tortuosities.

58 To evaluate the tortuosity in clay, it is important to understand the relation of the macrostructures  
59 of particles to macropores in clay layers. Previous studies have shown that in nature, smectite-type  
60 clays form clusters of several particles (Wong and Wang, 1997). Such clustering of particles may  
61 bring heterogeneity in pore size, anisotropy in the flow path (Olsen, 1962), and dead-end pores (Hong,  
62 2020), leading to complicated pore networks. In an attempt to assess how such intricate void  
63 structures influence the transport properties, Bacle et al. (2016) simulated various platelet structures  
64 and investigated the effects of structural differences on the diffusivity. They applied the Gay-Berne  
65 potential to platelets assumed to represent clays and estimated the diffusivity in macropores, but the  
66 validity of their analysis is unclear because their model allowed particles to overlap.

67 Further caution is needed to assess how pore networks facilitate mass transfer in clay layers  
68 containing particle clusters. In general, the width of interlayer spaces in clay clusters are on the  
69 nanometer scale, and it is unclear how such tiny gaps contribute to overall mass transport. For  
70 example, Bacle et al. (2016) analyzed the diffusion coefficient in platelet bed and noted that  
71 diffusivity within particle clusters is smaller than outside. Boğan et al. (2011) performed molecular

72 simulations assuming electrical interaction between clay particle surfaces and water molecules. They  
73 found that fluids cannot be regarded as a continuum in pores smaller than a few nanometers. There is  
74 thus evidence that transport phenomena in nanopores contrast with those in outer macropores and  
75 they might be treated differently. For example, Wong and Wang (1997) reported limited water flow  
76 through tiny pores in particle clusters that cannot be driven by the hydraulic gradient. In another  
77 example, Li et al. (2018) separated voids into inner pores (micropores in particle clusters) and outer  
78 pores (macropores between clusters). They evaluated the permeability in clays based on the outer  
79 pore characteristics alone, assuming that the mass transfer in inner pores was negligible.

80 If only outer pores affect mass transfer, as reported in previous studies, it is important to quantify  
81 geometric characteristics of macrostructures of particles, which influences macropore characteristics.  
82 Li et al. (2018) examined the aspect ratio and the orientation angle of particle clusters from existing  
83 experimental results in clay layers, which were estimated to be approximately 2 to 3 and 30 to 60  
84 degrees, respectively. Adams et al. (2013) observed resedimented clay structures with BSEM  
85 (Backscattered Scanning Electron Microscope). The two-dimensional assessment revealed that the  
86 aspect ratio of particle cluster was approximately 2 and the orientation angle was 30 to 50 degrees,  
87 respectively. However, the structure of clay particles depends on their formation processes, it is  
88 possible for various configurations to result even at a given density. Therefore, it is difficult to  
89 generalize the type of macroscopic structures in clay layers and their internal pore network.

90 In this study, various structures of platelet particles, particularly clustered and almost-stacked  
91 structures (e.g. Schneider et al., 2011), were simulated under simple assumptions to investigate the  
92 macropore characteristics in particle layers. The tortuosity in these structures was calculated from a  
93 random walk analysis. Furthermore, in comparison with the existing geometrical tortuosity model,  
94 the compatibility of differently-defined tortuosities and the applicability of the model were examined.  
95 Finally, the relationship between the diffusional tortuosity and macroscopic structures of clay  
96 particles were investigated by comparing the results with diffusion experiments in clay layers under  
97 specific density conditions, to gain physical insights of complicated diffusivity in clay, which has

98 been reported in previous studies.

99

## 100 **2. Numerical Method**

### 101 **2.1 Monte Carlo Analysis**

102 In order to evaluate pore characteristics in clay layers, the internal structure, i.e., the arrangement  
103 of clay particle have to be considered. However, details of actual clay structures have not been fully  
104 understood. Therefore, this study modeled clay particles as platelets and computed various particle  
105 structures with different density conditions using a Monte Carlo analysis, which was used to  
106 investigate the relationship between macroscopic particle structures and pore networks. In this section,  
107 the simulation method of platelet structures conducted in this study is described below.

108 Bentonite clays are mainly composed of montmorillonite particles that have charged surfaces. A  
109 number of analyses of clay structure have been performed to explore the interaction between such  
110 particles. For example, Dijkstra et al. (1997) performed structural analysis that assumed a quadrupole  
111 potential for infinitely thin platelets. They reported that platelets at low densities exhibited edge-to-  
112 face configurations and were locally aggregated into “house-of-cards” structures, similar to those  
113 observed in actual clay particles. In contrast, increasing density results in structures that approached  
114 a nematic state with a parallel platelet arrangement. However, there may be thought practical limits  
115 to calculations that assume certain electrical interactions in higher density conditions. Bacle et al.  
116 (2016) applied the Gay-Berne potential to platelets with a finite thickness. They calculated the high-  
117 density structures allowing for overlap of particles. Terada et al. (2018) performed a structural  
118 analysis by assuming the rigid-body potential on infinitely thin platelets and examined the consistency  
119 with those using a quadrupole potential at moderate to high density. As the density increased, nematic  
120 structures were confirmed to occur due to stacking of platelets by excluded volume effects. Their  
121 results suggested that the rigid-body potential would be applicable at high-density conditions.

122 In order to examine how macroscopic structures affect pore characteristics, a structural analysis  
123 of platelet particles was performed using a Monte Carlo method. The details of the analyses is similar

124 to those by Terada et al. (2018). The calculation methods for various structures at given density are  
125 described later. The rigid body potential was applied to infinitely thin platelets with diameter  $\sigma$ . The  
126 cubic calculation region was considered and periodic boundary conditions were applied in all  
127 directions. The size of the calculation region was chosen to be sufficiently large relative to the  
128 structural formations, with an edge size  $L$  that was four times larger than the particle diameter  $\sigma$ . By  
129 setting the number of platelets  $N = 1920, 3200, 4480, 6400, 9600$  and  $10880$ , the analyses were  
130 performed using values of the non-dimensional density  $N\sigma^3/L^3$  ranging from 30 to 170. To calculate  
131 the dry density, the platelet was assumed to be monodisperse montmorillonite with a diameter  $\sigma =$   
132  $320$  nm, a thickness  $d = 1$  nm and a density  $\rho = 2.7$  Mg/m<sup>3</sup>. The corresponding dry density conditions  
133  $\rho_d = \rho\pi\sigma^2dN/4L^3$  are ranging from 0.20 to 1.13 Mg/m<sup>3</sup>. In general, the range of dry densities of clays  
134 is considered from 0.2 Mg/m<sup>3</sup> to 2.0 Mg/m<sup>3</sup>. There are two reasons why the analyses were performed  
135 only for low to moderate density conditions. The first reason is that the Monte Carlo simulation at  
136 large density takes an enormous computation time, since the present analysis does not allow  
137 overlapping of particles. The second is that it is difficult to form different macrostructures of platelet  
138 particles, because the number of possible configuration states of particle is very few at large densities  
139 ( $>1.0$  Mg/m<sup>3</sup>) by excluded volume effect. However, the present analysis captures the discontinuous  
140 change of pore characteristics of platelet layers with the density increase, as described later.

141 The initial state was made by randomly generated platelet positions and normal vectors.  
142 Geometric calculations were used to verify the intersections of each particle to avoid overlap. The  
143 position and orientation of each particle were then updated by random numbers, and the post-  
144 transition state was determined based on the Metropolis method. In this step, particle intersection was  
145 checked to avoid overlap. The maximum movement per translation was set to  $\Delta r = 0.02\sigma$  and the  
146 maximum variation for each normal vector component was  $\Delta v = 0.02$ .

147 In this study, diverse structures under conditions of a given density were fabricated. Monte Carlo  
148 analysis is generally used to determine thermodynamic equilibrium states, so that even in simulations



149 with different initial platelet arrangements, they should in principle converge to a single equilibrium  
150 state. In practice, Terada et al. (2018) performed structural analyses at various density conditions and  
151 calculated a single equilibrium structure for each condition. However, structures that vary from the  
152 equilibrium states may form, depending on the number of particles and the initial configurations.  
153 Therefore, various metastable structures were computed in this study, in which configurational  
154 changes became minute when calculating equilibrium states. Fig.1 shows examples of metastable  
155 structures of platelet system. 3D snapshots and cross-sectional views of platelet with different initial  
156 conditions at the same density are shown in Figs. 1(a) and (c). The Monte Carlo analysis conducted  
157 from these initial states yielded metastable structures, particularly clustered and almost-stacked  
158 structures (e.g. Schneider et al., 2011), which are shown in Figs. 1 (b) and (d).

159 In Fig. 1 (a), platelet angles were randomly assigned with the maximum angle  $\theta_{ni}=84.3$  degree  
160 ( $\cos \theta_{ni}=0.1$ ) from the vertical direction in the initial state. Under these conditions, the platelets may  
161 be random at first, but random placement is significantly restricted when the number of platelets  
162 increases as much as excluded volume of each particle overlaps. Consequently, the particles are  
163 repositioned along with other platelets without assuming any specific potential. When the Monte  
164 Carlo simulation was started from these initial conditions, each particle moves seeking to increase  
165 the number of possible states at first, but the structures cease to change after plenty of Monte Carlo  
166 steps (Fig. 1b). That is, the structures other than the equilibrium states may form during the  
167 computation process depending on initial configurations. Such states are considered as metastable  
168 structures and they are defined as one with sufficiently little configurational change after a sufficient  
169 number of steps. Fig. 1(c) shows the initial platelet structure in which the initial orientation limiting  
170 angle was  $\theta_{ni}=25.8$  degree ( $\cos \theta_{ni}=0.9$ ). Calculations starting from this state produced a metastable  
171 structure with laminated platelets (Fig. 1d). It is an entirely distinct structure compared to that shown  
172 in Fig.1(b), although they are the same density conditions. In this way, platelet structures with  
173 different internal configurations were fabricated.

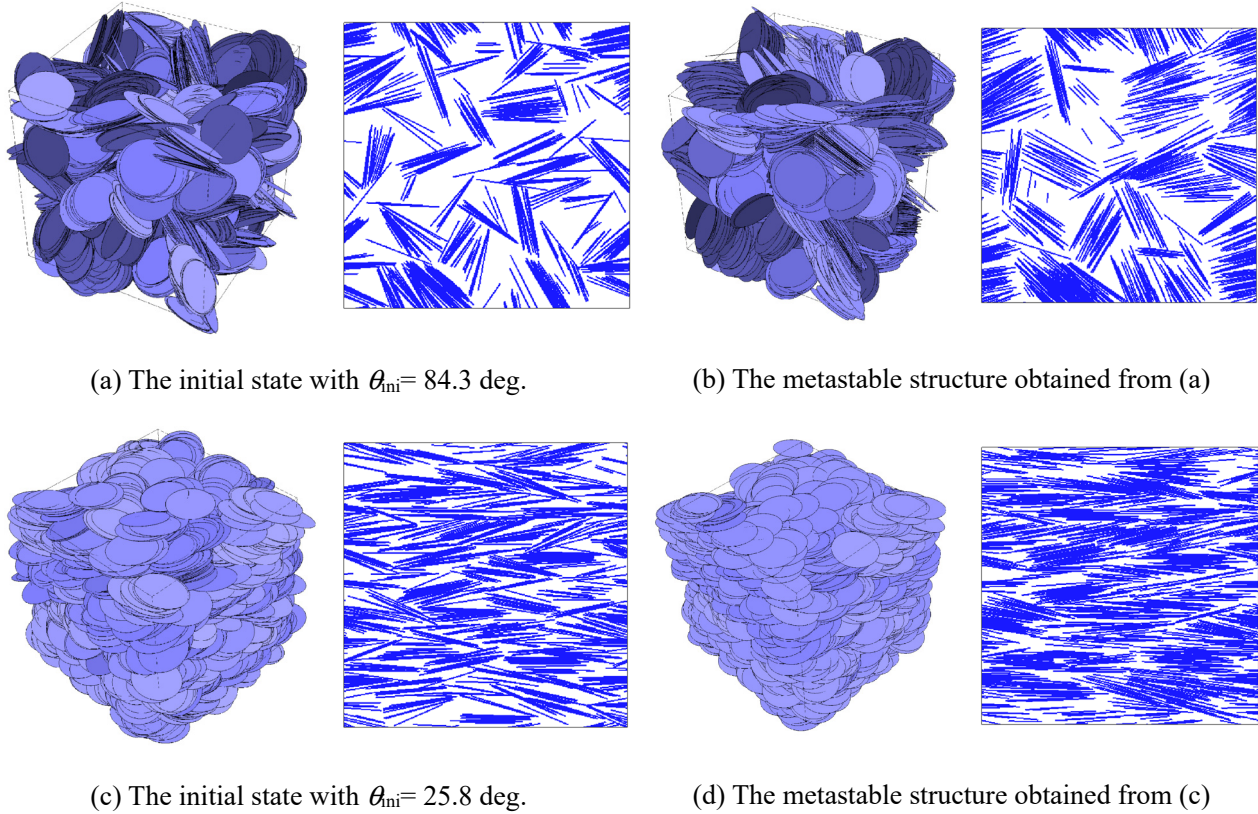


Fig. 1 3D snapshots and cross-sectional views of initial and metastable structures at a dry density of  $0.33 \text{ Mg/m}^3$ .

174

## 175 2.2 Extraction of Macropores

176 This study examined the influence of platelet structures on the macropore contributions to mass  
 177 transport. As mentioned above, it is known that clay particles form clusters in nature. To capture the  
 178 features of the macropores in such clusterized platelet structures, it is essential to investigate whether  
 179 nanometer-sized micropores within particle clusters influence the overall mass transfer.

180 In previous studies, Wong and Wang (1997) distinguished water in clay layers as free water or  
 181 intra-cluster water, where the former was present in macropores and could move along hydraulic  
 182 gradients, whereas the latter occurred within particle clusters, and had restricted flow. Similarly, Li et  
 183 al. (2018) separated the inner pores (inside particle clusters) from external pores and they categorized  
 184 inner pores as solid phases and estimated the clay permeability solely from external pores.  
 185 Nevertheless, it is challenging to precisely distinguish such pore types in clays. For example, mass  
 186 transfer may differ depending on the width of the flow path and the size of molecules, with molecules  
 187 behaving individually or collectively, similarly to the Knudsen flow for gases. In terms of pore

188 networks, it is also unclear whether molecules in dead-end pores affect the overall mass transfer or  
189 fluid permeability (Hong, 2020). In addition, electrical interaction problems may arise from the  
190 formation of immobile water layers (Singh and Wallender, 2008) that can impede the motion of  
191 molecules. Thus, it is difficult to estimate the distinguished pores that contribute to transport  
192 phenomena from those that do not.

193 To provide a clue to these issues, Boğan et al. (2011) numerically evaluated the width of flow  
194 paths in which fluids can be regarded as continuous. Specifically, they performed molecular dynamics  
195 simulations of water in clay nanopores in which electrical interactions were assumed and presented  
196 the results of fluid velocity and viscosity for various micropore widths. They concluded that fluids  
197 could be regarded as continuous for pore widths of 3 nm or more if slip boundary conditions were  
198 assumed. However, the velocity distribution results indicated that Poiseuille flow disturbed near the  
199 surface even for pore widths of 6 nm. These findings suggest that 3 nm to 6 nm may be the minimum  
200 pore width for a fluid continuum.

201 Like previous studies, this study assumed that nanometer-sized micropores do not contribute to  
202 transport phenomena in the context of continuous transfer. However, as described above, it is not easy  
203 to distinguish between inner and outer pores strictly based on physical evidence. For this reason, the  
204 analysis in this study did not classify inner and outer pores and extracted macropores by void size  
205 only. Specifically, we conducted a local averaging procedure that “filled” the space of a few  
206 nanometers from the particle surfaces to obtain macropores. The filling width was approximately 3  
207 to 6 nm, based on the results by Boğan et al. (2011). The detailed procedures are described as follows.

208 Macropores in a metastable platelet structure obtained by a Monte Carlo analysis were sterically  
209 isolated. First, the cubic calculation region was divided into  $400 \times 400 \times 400$  elements and a particle  
210 existence function  $\rho(x, y, z)$  (= 0 or 1) was mapped for each voxel. Next, a local averaging was  
211 performed on the particle existence function to calculate the continuous particle concentration fields.  
212 This operation excludes tiny pores between platelets that do not contribute to mass transfer. In this  
213 study, the following three-dimensional Gaussian function was used as a weight function of the local

214 averaging:

$$g(x, y, z) = \frac{1}{(2\pi\lambda^2)^{\frac{3}{2}}} \exp\left(-\frac{x^2 + y^2 + z^2}{2\lambda^2}\right) \quad (1)$$

215 where  $\lambda$  is the deviation parameter that determines the extent of the local averaging. Using Eq. (1),  
216 the particle concentration fields  $c(x, y, z)$  were calculated as follows:

$$c(x, y, z) = \int_{-\infty}^{\infty} g(x-x', y-y', z-z')\rho(x', y', z')dx'dy'dz' \quad (2)$$

217 The kernel size of each voxel was  $5 \times 5 \times 5$ , and voxels with particle concentrations of less than 0.001  
218 were regarded as voids. Figure 2 shows the calculation results of the local-averaged particle  
219 concentration field along with some values of the deviation parameter  $\lambda$ . The black areas represent  
220 voids while the bright areas are solid phases. For a small  $\lambda$  value (Fig. 2a), each platelet existed  
221 individually with tiny pores present between particles. However, large  $\lambda$  values (Fig. 2c) “filled” the  
222 spaces between particle layers to eliminate micropores. Thus, the parameter selection is significant  
223 because the voids extracted from the results differ substantially. In this study, an optimal deviation  
224 parameter was decided as  $\lambda = 0.003$ , which corresponds to the extraction of micropores with a width  
225 of 3 nm to 6 nm. By the local averaging, micropores in particle clusters was filled, consistent with  
226 previous studies that assumed that interlayer pores do not contribute to mass transfer in clays (Wong  
227 and Wang, 1997; Li et al., 2018). It is noted that the exclusion of micropore does not result in the  
228 fragmentation of macropores, as described later.

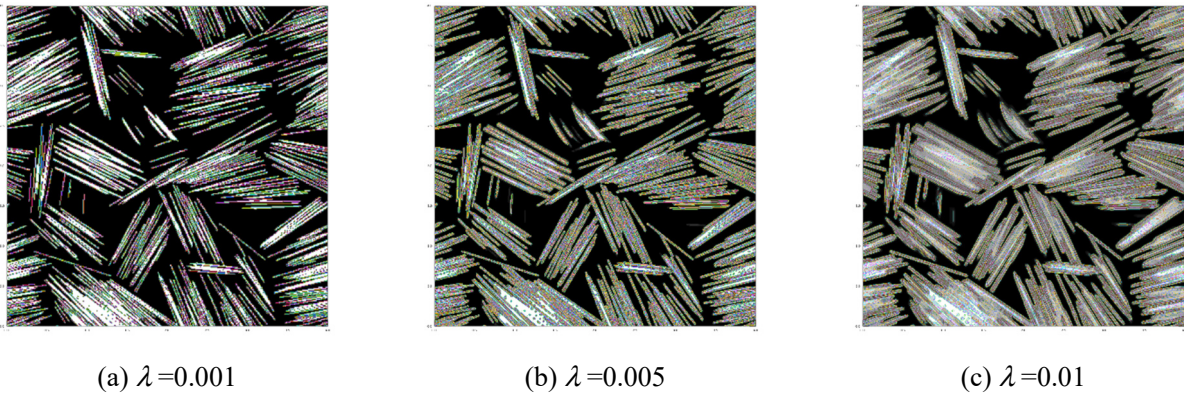


Fig. 2 Particle concentration fields of metastable structure after local averaging with various deviation parameters  $\lambda$ .

### 229 **2.3 Random Walk Analysis**

230 In order to characterize the pores in terms of tortuosity, random walk analyses for various  
231 metastable structures were performed. The tortuosity represents the sinuosity and complexity of voids  
232 and has been previously used in various engineering fields. Intuitively, the tortuosity is expressed as  
233 the ratio of the pore channel length  $L_e$  to the length  $L$  along the flow direction in porous media. While  
234 "hydrological" tortuosity was originally introduced to describe fluid permeation (Carman, 1937),  
235 tortuosities with different definitions have been used when evaluating other transport properties  
236 (Clennell, 1997). For example, "diffusional" tortuosity (Satterfield and Sherwood, 1963), which is  
237 related to molecular diffusion, "electrical" tortuosity (Tye, 1983), which describes electrical  
238 conduction, and "geometrical" tortuosity (Adler, 1992), which characterizes the microstructure of  
239 porous media, have been defined. The compatibility of these tortuosities has not been well understood.  
240 Ghanbarian et al. (2013), for example, reviewed existing models and their compatibility of  
241 differently-defined tortuosities. Fu et al. (2021) classified various types of tortuosities into physical  
242 and geometrical ones. The former describes different transport processes in porous media, including  
243 hydraulic, electrical, diffusional, and thermal tortuosity, while the latter characterizes the  
244 morphological properties of pore structures. They investigated the compatibility of such properties in  
245 sandstones composed of isotropic particles. The results suggested differences between physical and  
246 geometrical tortuosities, and in some cases, a comparison among physical tortuosities may even  
247 reveal different values. In addition, the tortuosity of particle layers is highly dependent on the  
248 microstructure, such as the size, shape, orientation, and spatial distribution of particles and voids  
249 (Vervoort and Cattle, 2003), and the results may differ significantly depending on the system under  
250 investigation.

251 In this study, the "diffusional" tortuosity in platelet layers in the compaction direction was  
252 calculated from the results of random walk analyses. In general, diffusion in porous media, such as  
253 rocks and clays, is strongly influenced by complicated geometric void structures, such as porosity  
254 and tortuosity. The relationship between the apparent diffusion coefficient  $D_a$  in a porous medium

255 and the self-diffusion coefficient  $D_0$  in free water was proposed (García-Gutiérrez, 2004):

$$D_a = \frac{\phi}{\phi + \rho_d K_d} \frac{\delta}{\tau_d^2} D_0 \quad (3)$$

256 where  $\phi$  is the porosity,  $\rho_d$  is the dry density,  $K_d$  is the distribution coefficient,  $\delta$  is the constrictivity,  
257 and  $\tau_d$  is the diffusional tortuosity. The constrictivity is a parameter that characterizes the so-called  
258 bottleneck effect in porous media (Holzer et al. 2013; Keller et al. 2015). As indicated in Eq.(3), the  
259 diffusion coefficient is a linear function of the constrictivity, while it is inversely proportional to the  
260 square of the tortuosity. In this study,  $\delta$  was simply assumed to be 1, because the tortuosity shows a  
261 large value in the platelet system, as described later. Furthermore, in the case of non-sorbing diffusion,  
262  $K_d$  can be regarded as 0. Therefore, the apparent diffusion coefficient  $D_a$  and the self-diffusion  
263 coefficient  $D_0$  can be represented using the diffusional tortuosity  $\tau_d$  as follows:

$$\frac{D_a}{D_0} = \frac{1}{\tau_d^2} \quad (4)$$

264 In general, molecular diffusion is governed by the Langevin equation or the Fokker-Planck  
265 equation and is sometimes analyzed using a random walk model, in which the mean-square  
266 displacement of many walkers at the long-time limit is proportional to the number of time steps.  
267 random walk analyses in macropores in platelet layers were calculated to statistically calculate the  
268 diffusion coefficient and the tortuosity via Eq. (4). The analyses were performed by similar method  
269 to Fu et al. (2021). The first step is to randomly place several walkers in voids at the initial state ( $t =$   
270  $0$ ). Then the walker positions are updated to selected neighboring voxels by random numbers. The  
271 walker position remains constant if the selected voxel is a solid phase. Repeating these steps yields  
272 the mean-square displacement with increasing time steps. Fu et al. (2021) computed the tortuosity of  
273 pores in sandstones in all  $x$ ,  $y$ , and  $z$  directions. Such calculations are practical for isotropic systems  
274 with relatively straight flow paths, however, platelet structures have large bending channels and  
275 consequently the tortuosity varies greatly depending on the direction. The tortuosity was calculated  
276 from the mean-square displacement of walkers (from bottom to the top of Fig. 3). The mean-square  
277 displacement in  $z$  direction in free space where all regions are voids can be expressed as follows:

$$\langle z^2(t) \rangle_{\text{free}} = \frac{1}{N} \sum_{i=1}^N [z_i(t) - z_i(0)]^2 \quad (5)$$

278 where  $N$  is the number of random walkers,  $z_i(t)$  is the position of the  $i$ -th walker at a given time, and  
 279  $\langle \rangle$  represents the ensemble average. The self-diffusion coefficient  $D_0$  can be calculated from the  
 280 mean-square displacement by the following equation.

$$D_0 = \frac{1}{2} \frac{d \langle z^2(t) \rangle_{\text{free}}}{dt} \quad (6)$$

281 Similarly, for random walkers in pore spaces, the mean square displacement in  $z$  direction  
 282 (compaction direction of platelets) and the apparent diffusion coefficient  $D_a$  can be expressed as  
 283 follows:

$$\langle z^2(t) \rangle_{\text{pore}} = \frac{1}{N} \sum_{i=1}^N [z_i(t) - z_i(0)]^2 \quad (7)$$

$$D_a = \frac{1}{2} \frac{d \langle z^2(t) \rangle_{\text{pore}}}{dt} \quad (8)$$

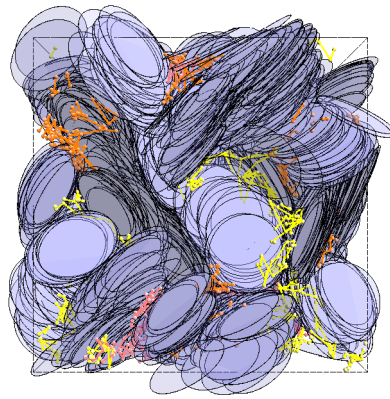
284 The diffusional tortuosity  $\tau_{dz}$  in  $z$  direction can be expressed from these ratios using Eqs. (6) and (8).

$$\tau_{dz} = \sqrt{\frac{D_0}{D_a}} = \sqrt{\frac{d \langle z^2(t) \rangle_{\text{free}} / dt}{d \langle z^2(t) \rangle_{\text{pore}} / dt}} \quad (9)$$

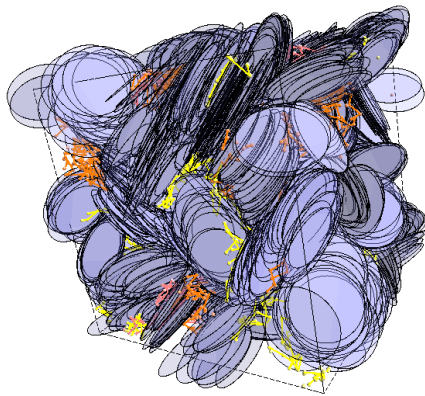
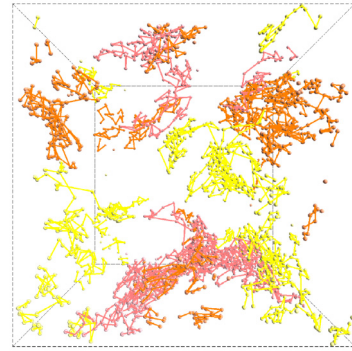
285 The calculation was performed over 10,000,000 time steps with 10,000 random walkers. Periodic  
 286 boundary conditions were applied in the analysis. Figure 3 indicates the trajectories of three random  
 287 walkers over 500,000 time steps as examples. The positions at each of the 500,000 time steps are  
 288 shown as spheres connected by lines. At first glance, the three trajectories appear to be disconnected,  
 289 but in fact they are all connected. This is because the trajectories that cross periodic boundaries are  
 290 not connected by lines for the sake of clarity. Therefore the trajectories of walkers moving back and  
 291 forth near the periodic boundary appear to be isolated.

292 As can be seen in Fig. 3 (a), walkers move between clustered platelets at random. This indicates  
 293 that the relatively large macropores between clusters, which can be visually confirmed, are connected

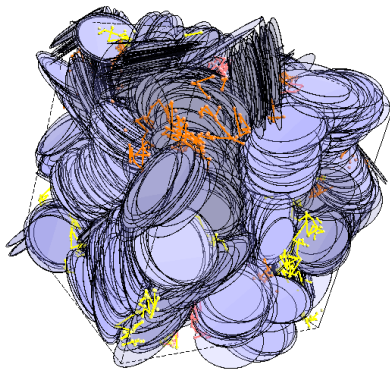
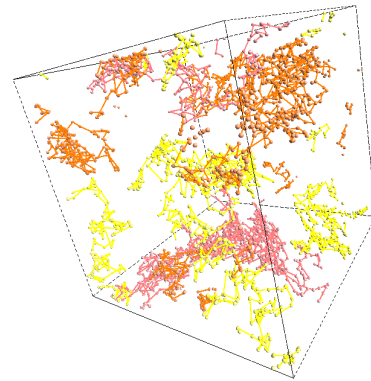




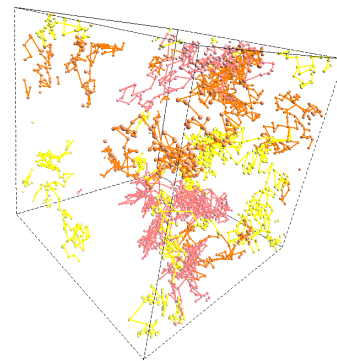
(a) viewpoint #1



(b) viewpoint #2



(c) viewpoint #3



294 Fig. 3 Random walker trajectories observed from different viewpoints; (left) overview, (right) trajectories.  
 295 Trajectories of three walkers are indicated as examples. For the sake of clarity, trajectories that cross periodic  
 296 boundaries are not connected by lines.  
 297

298 in three dimensions, allowing walkers to pass through them sufficiently. From checking the walker  
 299 trajectories, it was confirmed that macropore is not fragmented by the exclusion of micropores in the  
 300 process of the local averaging. In order to recognize the trajectory easily, Fig.3(b) shows the  
 301 trajectories of three random walkers without indication of platelets. As shown in Fig.3 (b), there was  
 302 sufficient movement in the computational domain even during 500,000 time steps.



303

## 304 **2.4 Cluster Judgement**

305 Because macroscopic configurations of clay particles are highly complicated and often unclear,  
306 various efforts have been made to quantitatively evaluate clay structures. Adams et al. (2013)  
307 conducted BSEM characterization of resedimented mudstones to estimate particle structures from  
308 image analysis. Their two-dimensional evaluations found a particle cluster aspect ratio of  
309 approximately 2 with orientation angles of approximately 30 to 50 degrees. Li et al. (2018) developed  
310 a theoretical model relating the angle and size of particle clusters to evaluate permeability in a  
311 smectite mudstone. Based on the previous study of clay swelling (Wong and Wang, 1997), they  
312 constructed a model relating particle angles to porosity and applied their model to mudstones used in  
313 previous studies (Gautam, 2004; Chalindar, 2010; Schneider et al., 2011), for which they obtained  
314 the angle and aspect ratio of particle clusters. According to the summarized data, the orientation angle  
315 of the smectite mudstone was approximately 30 to 60 degrees with a cluster aspect ratio around 2 to  
316 3. Although the validity of these values still needs to be verified, it underscores the importance of  
317 knowing the size and configuration of clusters in order to estimate particle structures in clay  
318 quantitatively.

319 In order to evaluate the shape and size of particle clusters in the metastable structures obtained by  
320 Monte Carlo analysis quantitatively, a cluster judgment of platelets was performed. This judgment  
321 determined the clusters to which each platelet belonged, using procedures similar to those by  
322 Wouterse et al. (2007). Firstly, candidate particles that could form the center of each cluster were  
323 identified. The location vectors of particles  $i$  and  $j$  are  $\mathbf{r}_i$  and  $\mathbf{r}_j$ , and the normal vectors are  $\mathbf{u}_i$  and  $\mathbf{u}_j$ ,  
324 respectively. The correlation of the normal vector with adjacent particles at each particle location was  
325 then calculated using a normalized Gaussian function as follows:

$$c(\mathbf{r}_i) = \sum_{j \neq i}^N \exp \left[ -\frac{(\mathbf{r}_i - \mathbf{r}_j)^2}{2\alpha^2} \right] (\mathbf{u}_i \cdot \mathbf{u}_j) \quad (10)$$

326 where  $\alpha$  is the spread of correlation. The particles were then sorted at the highest  $C(\mathbf{r}_i)$  value, selecting

327 higher particles as candidates for the center of each cluster. Furthermore, we verified whether the  
 328 particle orientation was aligned from Eq. (11), whether the normal distance between particles was  
 329 close using Eq. (12), and whether the tangential distance between particles was small using Eq. (13)  
 330 for candidate particles and adjacent particles:

$$|\mathbf{u}_i \cdot \mathbf{u}_j| > 1 - \delta_{pc} \quad (11)$$

$$|(\mathbf{r}_i - \mathbf{r}_j) \cdot \mathbf{u}_j| < \delta_{nc} \quad (12)$$

$$\frac{1}{2}|(\mathbf{r}_i - \mathbf{r}_j) - (\mathbf{r}_i - \mathbf{r}_j) \cdot \mathbf{u}_i \mathbf{u}_i| + \frac{1}{2}|(\mathbf{r}_i - \mathbf{r}_j) - (\mathbf{r}_i - \mathbf{r}_j) \cdot \mathbf{u}_j \mathbf{u}_j| < \delta_{sc} \quad (13)$$

331 where  $\delta_{pc}$ ,  $\delta_{nc}$ , and  $\delta_{sc}$  are the cluster judgment parameters and  $\delta_{pc} = 0.06$ ,  $0.075\sigma < \delta_{nc} < 1.0\sigma$ , and  
 332  $0.2\sigma < \delta_{sc} < 0.25\sigma$ , respectively ( $\sigma$ : platelet diameter). Figure 4 shows an example of the cluster  
 333 judgment results for a metastable structure at a dry density of  $0.33 \text{ Mg/m}^3$ . In the figure, platelet  
 334 particles identified as the same cluster are shown in identical colors and isolated platelets are shown  
 335 in black. As shown in Fig.4, clusters of different size and orientation can be observed in a single  
 336 platelet structure. These cluster characterizations make it possible not only to clearly visualize the  
 337 structural properties but also to quantitatively estimated of cluster geometric properties such as the  
 338 aspect ratio. The details of the calculation method for the aspect ratio is described below.

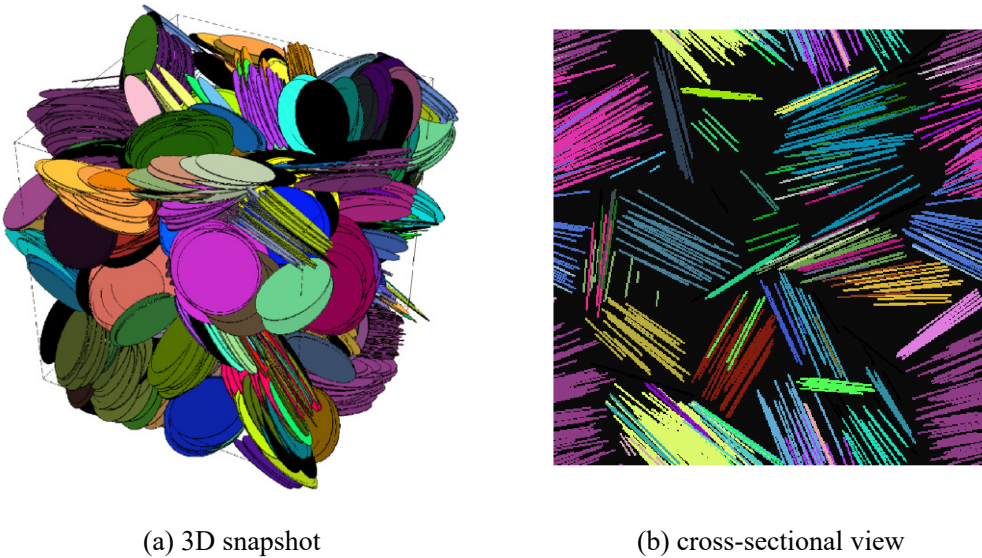


Fig. 4 Cluster judgement for metastable structure at dry density  $0.33 \text{ Mg/m}^3$ .

### 339 **3. Results and Discussion**

#### 340 **3.1 Platelet Structures from Monte Carlo Analysis**

341 This aim of this study is to investigate the influence of platelet configurations on pore networks  
342 and their contribution to mass transfer. In order to obtain metastable structures with differing internal  
343 geometries, Monte Carlo analyses were performed under various initial conditions. Then macropores  
344 in the platelet structures were isolated by local averaging procedures. Figure 5 shows partial cross-  
345 sectional views of macropores (white part) and solid phase with micropore (blue part) for various  
346 platelet structures (dry density from 0.20 to 1.13 Mg/m<sup>3</sup>). As seen in the figure, various platelet  
347 structures are fabricated even at the same dry density by the Monte Carlo analyses with different  
348 initial configurations. If the initial orientation angle of the platelets is large, only a few possible  
349 particle states exist at a high density and a considerable amount of time is required to randomly  
350 arrange the particles. Accordingly, only a stacked structure is shown for conditions with dry densities  
351 greater than 0.99 Mg/m<sup>3</sup> in Fig.5.

352 The characteristics of the solid phases with micropores (blue part) reveal that the size and angle of  
353 platelet clusters are entirely different for the various initial states at each density condition. For  
354 example, when the initial orientation angle limit was large, platelets became aggregated into clusters  
355 of various sizes and angles, while smaller initial angles produced flat clusters with aligned  
356 orientations. Of course, it is unknown which structures are similar to those of actual clay layers at this  
357 stage. Concerning macropores (white part), large voids are connected between clusters in the  
358 structures containing large-angled clusters (upper column), constituting pore networks that extend in  
359 various directions. Although the macropores appear to be partially isolated in the 2D cross-sectional  
360 view, the random walk analysis confirmed that they are connected in 3D. In the structures with small-  
361 angled clusters (lower column), tiny voids are connected along the lamination direction of the  
362 platelets and pore networks exhibit significant anisotropy.

363 The discussion given here highlights how remarkably different pore characteristics can develop  
364 depending on the macroscopic structural properties of particles, such as size and orientation of.

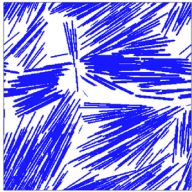
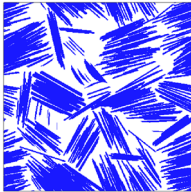
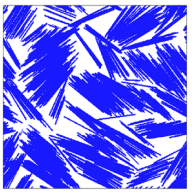
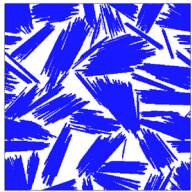

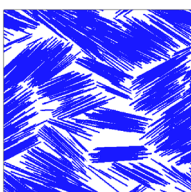
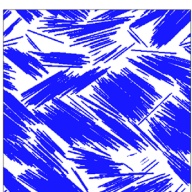
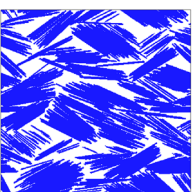
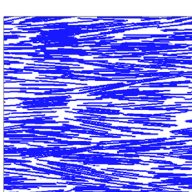


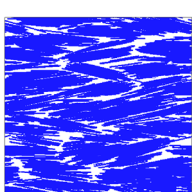
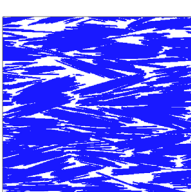
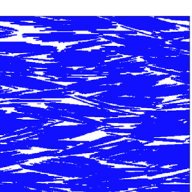
| $\rho_d=0.20 \text{ Mg/m}^3$  | $\rho_d=0.33 \text{ Mg/m}^3$  | $\rho_d=0.46 \text{ Mg/m}^3$  | $\rho_d=0.66 \text{ Mg/m}^3$   | $\rho_d=0.99 \text{ Mg/m}^3$  | $\rho_d=1.13 \text{ Mg/m}^3$  |
|---|---|---|--|---|---|
|  |  |  |  |   |   |
| (I)   | (IV)  | (VII)   | (X)  |   |   |
|  |  |  |  |   |   |
| (II)  | (V)   | (VIII)  | (XI)   |   |   |
|  |  |  |  |  |  |
| (III)   | (VI)  | (IX)  | (XII)  | (XIII)  | (XIV)   |

Fig. 5 Results of extraction of macropores in metastable structures at various density conditions. The white part represents macropores and the blue part is solid phase with micropores. The initial orientation limiting angle  $\theta_{mi}$  =84.3 deg. (upper), 60.0 deg. (middle) and 25.8 deg. (lower), respectively.

365 clusters These results may significantly influence the tortuosity which represents the sinuosity and  
366 complexity of voids. The above results implies the importance of knowing the macroscopic internal  
367 structures, including macropores, on estimating transport properties in clay layers. It should be noted  
368 again that, it is not clear which platelet structure represents actual clay layers because the  
369 macrostructures of clay are still unspecified at respective density conditions.

370

### 371 3.2. Tortuosity from Random Walk Analysis

372 Considering that the pore characteristics are affected by macrostructural differences within  
373 platelet structures, the tortuosity also varies with the internal structure under the same density  
374 conditions. In this section, the relationship between the tortuosity from a random walk analysis and  
375 the platelet structure is discussed. The mean-square displacements of walkers in one direction ( $z$   
376 direction) were computed from a three-dimensional random walk simulation both in macropores of

377 platelet structures and free space. The tortuosity can be obtained by substituting these results into Eq.  
 378 (9). It corresponds to “diffusional” tortuosity among various definitions of tortuosity as described  
 379 above.

380 Table 1 shows the diffusional tortuosity in the  $z$  direction  $\tau_{dz}$  determined by a random walk  
 381 simulation. The roman numerals in the table correspond to the metastable structure numbers (see Fig.  
 382 5). The effective porosity  $\phi_e$ , the average orientation angle  $\theta_{fa}$ , and the aspect ratio of the particle  
 383 clusters  $m_{eq}$  for each platelet structure are also summarized. These values are needed to compare the  
 384 results with the existing tortuosity model, as given in the later section. The specific methods used to  
 385 calculate  $m_{eq}$  and  $\theta_{fa}$  are also described later.

386 The effective porosity  $\phi_e$  was calculated by computing the percentage of void voxels after the  
 387 local averaging procedure, in which macropores were obtained by “filling” nanopores. It corresponds  
 388 to the ratio of “external” pore volume which contribute to mass transfer in clays if the assumptions  
 389 are valid (Wong and Wang, 1997; Li et al., 2018). Table 1 indicates that the effective porosity  
 390 decreases as particle density increases and varies somewhat with the structures even at the same  
 391 density condition. It is especially small in the stacked structures (see the lower column of Fig.

392 Table 1 Various structural and pore characteristics for each metastable structure

| Structure number | Diffusional tortuosity $\tau_{dz}$ (-) | Effective porosity $\phi_e$ (-) | Average orientation angle $\theta_{fa}$ (deg.) | Aspect ratio of particle clusters $m_{eq}$ (-) |
|------------------|--|---------------------------------|--|--|
| (I)              | 1.58                                   | 0.52                            | 57.4   | 2.93   |
| (II)             | 2.34                                   | 0.49                            | 30.1   | 2.85   |
| (III)            | 6.11                                   | 0.43                            | 6.9  | 7.38   |
| (IV)             | 1.71                                   | 0.42                            | 54.6   | 2.95   |
| (V)              | 2.18                                   | 0.39                            | 35.7   | 3.17   |
| (VI)             | 5.60                                   | 0.31                            | 10.0   | 6.05   |
| (VII)            | 1.75                                   | 0.38                            | 52.5   | 2.57   |
| (VIII)           | 2.08                                   | 0.36                            | 40.8   | 3.15   |
| (IX)             | 5.53                                   | 0.26                            | 11.5   | 5.75   |
| (X)              | 1.77                                   | 0.33                            | 55.4   | 2.05   |
| (XI)             | 2.26                                   | 0.31                            | 40.8   | 2.65   |
| (XII)            | 5.97                                   | 0.20                            | 12.5   | 5.63   |
| (XIII)           | 6.07                                   | 0.19                            | 12.8   | 5.80   |
| <b>(XIV)</b>     | <b>6.85</b>                            | <b>0.20</b>                     | <b>12.6</b>                                    | <b>5.71</b>                                    |

393

394 5), because many tiny pores present between platelet clusters. Estimating the effective porosity in  
395 actual clays is not easy because its definition is somewhat arbitrary. A few previous studies have  
396 attempted to determine it, such as Li et al. (2018), who reported that the effective porosity of natural  
397 smectite clays is approximately 0.25 to 0.6. The present results agree with their findings reasonably,  
398 supporting the validity of the local averaging procedure used here.

399 Next the diffusional tortuosity  $\tau_{dz}$  which is shown in Table 1 is discussed. As is well-known, the  
400 tortuosity in clay layers shows the anisotropy (Keller et al., 2011). However only the tortuosity  
401 perpendicular to the platelet orientation (platelet compaction direction) was considered in this study.  
402 Under the calculation conditions, the tortuosity obtained from a random walk simulation is  
403 approximately from 1.5 to 6.0. As described earlier, the tortuosity is expressed as the ratio of flow  
404 path length to the system length geometrically. Compared these values with the observation of white  
405 part in Fig.5, the results shown here are intuitively agreement with the geometrical definition of  
406 tortuosity. For example, the geometrical tortuosity (pore length relative to system length) can be  
407 visually estimated as approximately 1 to 2 in platelet structure X (see white areas in Fig. 5), while the  
408 diffusional tortuosity  $\tau_{dz} = 1.77$ . Conversely, pores in platelet structure XII has substantial curvature,  
409 while the diffusional tortuosity  $\tau_{dz} = 5.97$  in this structure. Although the discussion given here is  
410 qualitative, the results given here suggest that the diffusional tortuosity sufficiently represents the  
411 geometrical tortuosity which is based on the curvature of flow path.

412 The effects of macroscopic particle cluster structures on tortuosity are summarized as follows. In  
413 the upper and middle structures shown in Fig. 5, particles formed relatively large clusters with small  
414 aspect ratios. As a result, the void channels exhibit little curvature and the tortuosities are accordingly  
415 small. Conversely, the lower structures in Fig. 5 contain flattened particle clusters with large aspect  
416 ratios with substantially bent pore networks, resulting in significantly large tortuosities. The tortuosity  
417 in the platelet structures varied by several times even at the same density conditions. It suggests that  
418 particle structures do greatly influence transport properties in platelet particles like clay layers.

419

### 420 3.3 Macrostructures in Platelet Particles from Cluster Judgement

421 Pore networks are greatly affected by the macroscopic configurations of particles, and it is  
422 therefore vital to quantify such structural properties, as done by Li et al. (2018), who estimated aspect  
423 ratios and orientation angles to characterize clay structures. Therefore, these parameters are evaluated  
424 to quantitatively describe the structural characteristics. As it is not clear which particles belong to the  
425 same cluster within the platelet structures shown in Fig. 5, the size and shape of the clusters could not  
426 be explicitly determined. Accordingly, a cluster judgment was performed for all metastable structures,  
427 which allowed us to examine the parameters mentioned above.

428 Figure 6 shows the results of the cluster judgment and geometric structural properties for platelet  
429 structures X, XI and XII at a dry density of 0.66 Mg/m<sup>3</sup>. Figs. 6 (a) and (b) indicates 3D snapshots  
430 and cross-sectional views of clustered platelets visualized by color. As shown in the figure, structures  
431 X and XI (upper and middle column) contain clusters which vary in size and orientation. In contrast,  
432 many flat clusters formed in the stacked structures XII (lower column), which had relatively uniform  
433 angles.

434 The aspect ratio (diameter/thickness) of each cluster was calculated to examine the size  
435 characteristics. Fig.6 (c) indicates histograms of the aspect ratios for the metastable structures. The  
436 results are only shown up to a value of 20. Structures X and XI (upper and middle column) had a  
437 large fraction of clusters with small aspect ratios, while few such clusters were found in structure XII  
438 (lower column), which had a relatively large number of clusters with large aspect ratios. Thus, entirely  
439 different cluster size features were observed even at the same density.

440 From the results of Fig.6(c), the averaged aspect ratio of each structures was calculated. Following  
441 the procedure of Daigle and Dugan (2011), the averaged aspect ratio  $m_{eq}$  is calculated as follows;

$$\frac{1}{m_{eq}} = \sum_{i=1}^n \frac{f_i}{m_i^2} \quad (14)$$

442 where  $f_i$  is the fraction of particles with an aspect ratio  $m_i$ . The averaged aspect ratios for each  
443 metastable structure are summarized in Table 1. Significant differences in cluster size can occur under

444 the same density conditions. Compared among the platelet structures shown in Fig.6, the values of  
 445  $m_{eq}$  are 2.05 for structure X, 2.65 for structure XI, and 5.63 for structure XII, respectively. These are  
 446 consistent with the aspect ratios of clusters observed visually from the cross-sectional views in Fig.  
 447 6 (b).

448 The platelet orientations are also evaluated by calculating the vertical orientation angles  $\theta$  of  
 449 platelets and then averaging them arithmetically. The histograms of orientation angles for structures  
 450 X, XI, and XII are shown in Fig. 6 (d). As seen in the figure, structure X displays considerable  
 451 variations in angle, but with a relatively uniform frequency with average angle  $\theta_a$  of 55.4 degree (see  
 452 Table 1). Structure XI exhibits a hill-like distribution with an average angle of 40.8 degrees. In  
 453 structure XII, approximately 70% of the platelets fell in the range of 10 to 20 degree with an average  
 454 angle of 12.5 degrees. These results demonstrate a wide variety of angle distributions that can result  
 455 even at a given density.

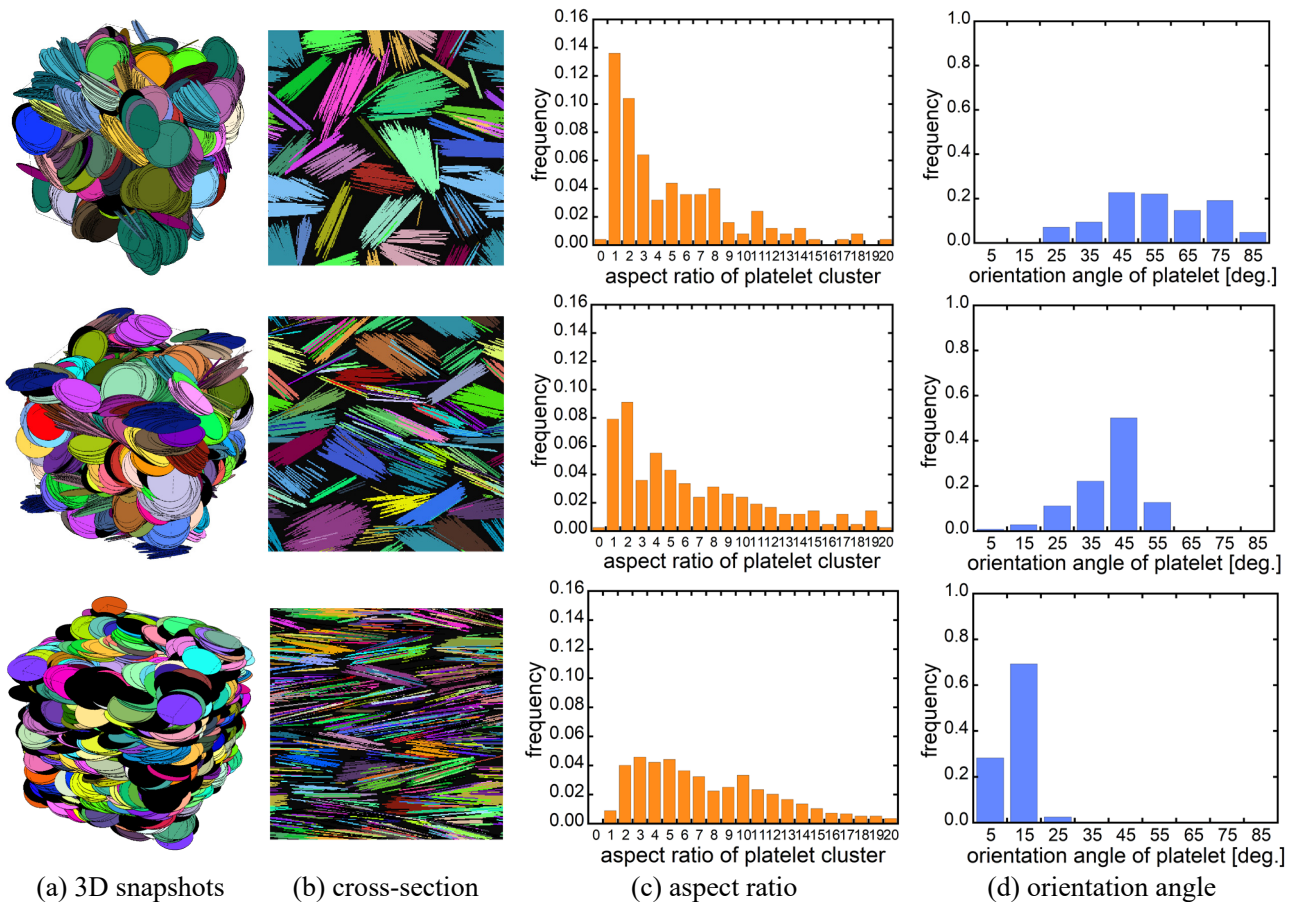


Fig. 6 Results of cluster judgment and geometrical structural properties for various platelet structures at dry density  $\rho_d=0.66 \text{ Mg/m}^3$ . Structural numbers are X (upper), XI (middle) and XII (lower), respectively.



456 In structures X and XI, which is shown in the upper and middle columns of Fig. 6, the averaged  
457 aspect ratio  $m_{eq}$  is approximately 2 to 3, and the average orientation angle  $\theta_a$  is approximately 50  
458 degrees. These structures are visually similar to those of clay layers described in previous studies (e.g.  
459 Pusch, 1983). More quantitatively, Li et al. (2018) reported that the aspect ratios and orientation  
460 angles of particle clusters in smectite clays are approximately 2 to 3 and 30 to 60 degrees, respectively.  
461 The clustered structures described here are again comparable with their findings, although speculative,  
462 this comparison suggests that such structures may be found in clay layers in nature.

463 In structure XII, which is shown in the lower column of Fig. 6, the averaged aspect ratio  $m_{eq}$  are  
464 approximately 6 and the orientation angle  $\theta_a$  are around 10 degree. As noted earlier, for particle  
465 density above a certain level, the number of possible states is reduced and it is difficult for clustered  
466 structures to form, so that stacked structures may better represent clays that have experienced  
467 compaction.

468

### 469 **3.4. Comparison with Tortuosity Model**

470 The previous sections demonstrated that configurational properties significantly affect the  
471 tortuosity in platelet layers. In order to predict the tortuosity in platelet layers quantitatively, it is  
472 important to characterize such macroscopic structures. This section refers to the existing tortuosity  
473 models of particulate beds and describes the necessary parameters for tortuosity models of platelet  
474 layers.

475 As previously described, tortuosities may be defined in different ways. For isotropic particle  
476 layers such as spherical particulate bed, various models have been developed to represent each type  
477 of tortuosity. For examples, Millington (1959) theoretically systematized diffusional tortuosity and  
478 Koponen et al. (1996) modeled hydraulic tortuosity. Various other models have also been proposed  
479 from different perspectives (Weissberg, 1963; Boudreau, 1996; Ahmadi et al., 2011). In most studies,  
480 tortuosity in spherical particle bed has described as a function of porosity alone. In other words, the  
481 effects of macroscopic structures on tortuosity are expected to be small for isotropic particle beds.

482 In contrast, tortuosity in platelet layers cannot easily be described solely in terms of porosity  
 483 because of the strong dependence on the macroscopic configuration. For example, Daigle and Dugan  
 484 (2011) proposed a geometrical tortuosity model in platelet structures based on simple assumptions:  
 485 they placed disk-shaped objects representing clay cluster at regularly spaced intervals and calculated  
 486 the lengths of macropores geometrically. The resultant model is described as follows:

$$\tau_{gz} = 1 + \frac{\frac{8m}{9} \cos\left(\frac{\theta_1 + \theta_2}{2}\right) + \sin\left(\frac{\theta_1 + \theta_2}{2}\right)}{\frac{3\pi}{8(1-\phi)} - \frac{1}{2}} \quad (15)$$

487 where  $\tau_{gz}$  is the geometrical tortuosity perpendicular to the platelet orientation,  $m$  is the aspect ratio  
 488 of the particle cluster,  $\phi$  is the porosity, and  $\theta_1$  and  $\theta_2$  represent the minimum and maximum  
 489 orientation angles, respectively. They compared this model with the results of hydraulic tortuosity  
 490 from lattice-Boltzmann simulations and confirmed the validity of their model. It means that they  
 491 suggested a correspondence between the hydraulic and geometrical tortuosities. They also performed  
 492 the geometric consideration of the tortuosity in polydispersed particle clusters using the averaged  
 493 aspect ratio described in Eq.(14).

494 However, it is unclear whether the model in Eq.(15) can be used to express the tortuosity in more  
 495 complicated structures. Therefore, the model validity was examined by comparing the diffusional  
 496 tortuosity from a random walk analysis with that from geometrical tortuosity model, and additionally  
 497 examined the influences of platelet structures to these tortuosities. Figure 7 shows comparisons  
 498 between the present analyses and the model by Daigle and Dugan (2011). The black lines represent  
 499 model results in which the averaged aspect ratio and orientation angle of each structure (see Table 1)  
 500 was substituted into Eq. (15), and the red plots represent the tortuosity obtained from random walk  
 501 analyses. As can be seen in Fig.7, the tortuosity increases gradually as porosity decreases and it varies  
 502 greatly depending on the structure even at the same density condition. For example, as shown in Fig.  
 503 7 (d), the tortuosities in structure X ranged from approximately 1 to 4, while those in structure XII  
 504 ranged from 1 to 9 even though the density conditions are the same. These variances are obviously

505 caused by complicated dependency of the tortuosity on macrostructural characteristics.

506 Fig.7 also shows that the tortuosities from the model and the present analysis are generally in good  
 507 agreement. However, the model results is slightly larger than that from the present analysis under  
 508 some conditions. One of the reasons might be the angle averaging. Daigle and Dugan (2011) estimated

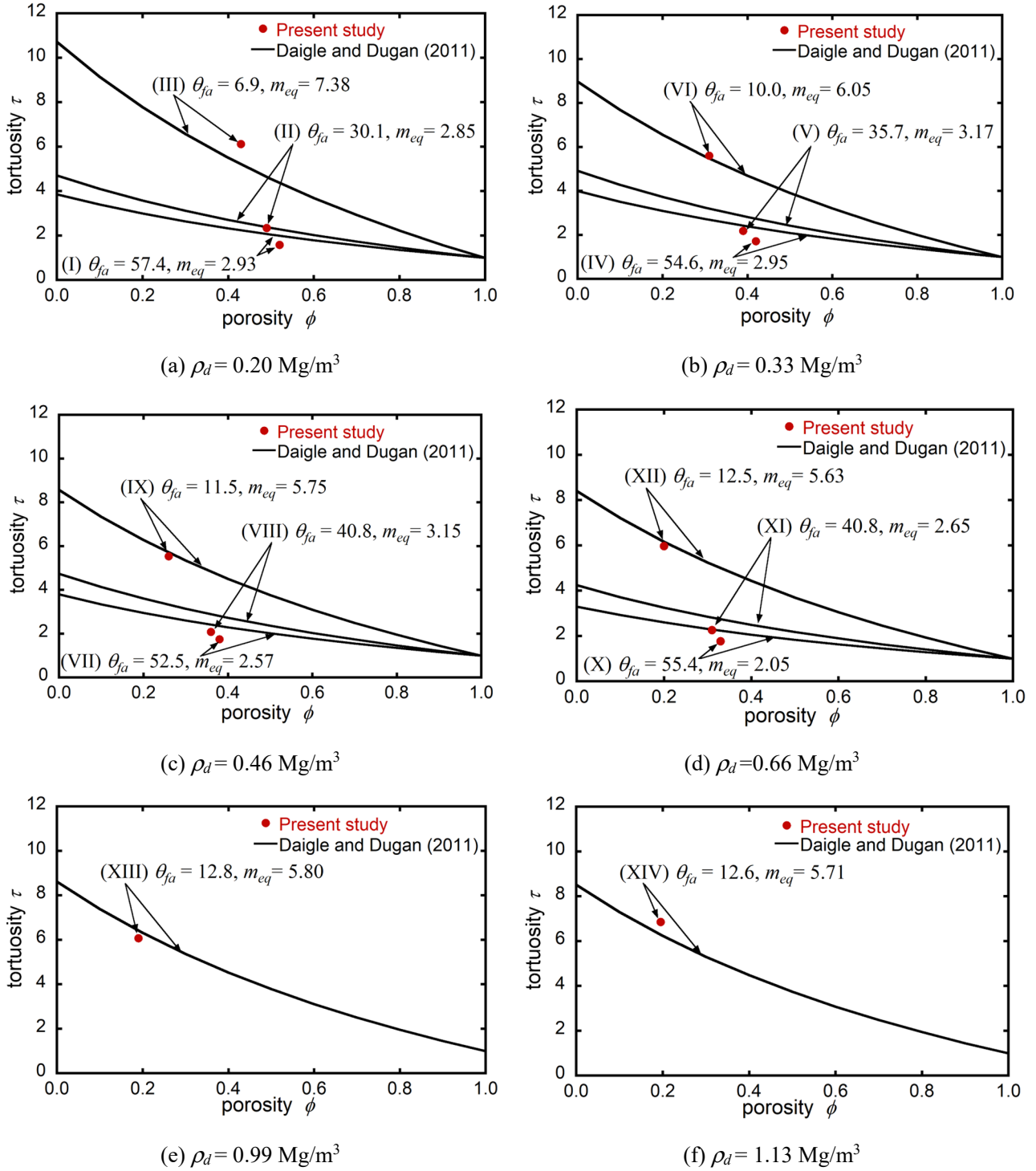


Fig. 7 Comparison of diffusional tortuosity and geometrical tortuosity model for each metastable structure.

509

510 the averaged angle from arithmetic average of minimum and maximum orientation angles, but  
511 actually the platelet angles have a wide range, as shown in Fig.6 (d). For example, the orientation  
512 angles ranges widely in clustered structures (see upper and middle columns of Fig. 6), suggesting that  
513 the above considerations may have produced differences between the model and the analysis. In  
514 contrast, stacked structures (see lower column of Fig. 6) exhibits only slight angle variations. In this  
515 case, the above effect is minor and the model results agree well with the results of random walk  
516 analysis. These results suggest as follows. First, the simple tortuosity model constructed by Daigle  
517 and Dugan (2011) could sufficiently evaluate the tortuosity in complex platelet structures for low to  
518 moderate density conditions. Their model expresses the tortuosity in both cluster and almost-stacked  
519 structures as shown in Fig.5. This implies that the model can be applied to more dense platelet layers  
520 with nematic structures, which is not shown here. Secondly, although the geometrical and diffusional  
521 tortuosities are defined differently, there might be a correspondence between them. Importantly, to  
522 estimate the tortuosity in platelet structures, it is vital to consider the macroscopic characteristics,  
523 such as the aspect ratio and the orientation angle of particle clusters.

524

### 525 **3.5 Comparison with Diffusion Experiments**

526 The diffusional tortuosity in the platelet structures was compared with the diffusion coefficient  
527 for actual clay layers. As described in Eq.(4), diffusional tortuosity is uniquely related to the diffusion  
528 coefficient of non-sorbing materials. Tritium (HTO) is used to experimentally determine diffusivity  
529 in clay layers without the influence of sorption effects. Bacle et al. (2016) summarized the relationship  
530 between dry density and diffusion coefficients from previous experiments in clay layers. Figure 8  
531 shows the diffusion coefficients of tritium in the same direction as clay consolidation from their cited  
532 data (Choi and Oscarson, 1996; García-Gutiérrez et al., 2004; Sato and Suzuki, 2003; Suzuki et al.,  
533 2004; González-Sánchez et al., 2008; Glaus et al., 2010; Tachi and Yotsuji, 2014; Melkior, 2009; Sato  
534 et al., 1992; Kozaki et al., 1999; Nakashima, 2004; Nakashima and Mitsumori, 2005; Nakashima,  
535 2001). The horizontal axis is dry density of clays and the vertical axis represents the ratio of the

536 apparent diffusion coefficient  $D_a$  to the self-diffusion coefficient  $D_0$ .

537 Experimental results in Fig. 8 indicate the complicated density dependency of the diffusion  
538 coefficient. At low density ( $\rho_d < 0.6 \text{ Mg/m}^3$ ), the diffusion coefficient monotonically decreases with  
539 increasing density. At moderate density ( $\rho_d > 0.6 \text{ Mg/m}^3$ ), the diffusion coefficient displays significant  
540 variations of around one order of magnitude for a given density. Bacle et al. (2016) numerically  
541 analyzed diffusion coefficients in clay layers in comparison with experimental results at various  
542 density conditions. They applied the Gay-Berne potential to thick plates and computed the results for  
543 high-density conditions. However, their structural analysis allowed for overlap between particles, and  
544 it is difficult to determine whether the macropores resulting from the excluded volume effect  
545 associated with the clustering of platelet particles were appropriately modeled.

546 The diffusional tortuosity in macropores formed by the excluded volume effect was compared  
547 with existing experimental results, similar to Bacle et al. (2016). The colored plots in Fig. 8 indicate  
548 the diffusion coefficient converted from the tortuosity of structures I to XIV obtained from a random  
549 walk analyses using Eq. (4). It should be noted that, all structures do not represent the actual structure  
550 of clay layers, because these are parametrically prepared in the analysis. At low density conditions  
551 ( $\rho_d = 0.20\text{--}0.46 \text{ Mg/m}^3$ ) shown in Fig. 8, the diffusion coefficient in stacked structures (structures III,  
552 VI and IX) differed strongly from the experimental results, while those for clustered structures  
553 (structures I, II, IV, V, VII and VIII) were in good agreement with the experiments.

554 As indicated in Table1, these clustered structures have the aspect ratio  $m_{eq}$  of around 2 to 4 and  
555 an orientation angle  $\theta_{fa}$  of 30 to 60 degree. These values are relatively consistent with smectite  
556 structures reported by Li et al. (2018). At high density ( $\rho_d = 0.66\text{--}1.13 \text{ Mg/m}^3$ ), the diffusion  
557 coefficient in stacked structures (structures XII, XIII and XIV) approaches those of the experiments.  
558 Such agreements indicate that the actual clay particles may have nematic structures under high density  
559 conditions that would increase the number of possible particle states.

560 These results suggest that the density dependence of the diffusivity in clay layers would result  
561 from the diversity of particle structures with anisotropic shapes. At low density conditions, only slight

562 variations in the diffusion coefficient from the experiments occur, which tend to decrease  
 563 monotonically. In this density range, the values are quantitatively consistent with the diffusion  
 564 coefficients in clustered structures, such as those found in common clay layers. However, at moderate  
 565 density conditions, the significant variations in the diffusion coefficient are quantitatively consistent  
 566 with the tortuosity in clustered structures at the upper limit and with the tortuosity in stacked structures  
 567 at the lower limit. As mentioned earlier, clay structures depend on the formation process and  
 568 conditions, therefore various internal structures are presumed to have formed under these density  
 569 conditions. The diffusion coefficients are expected to convert to the values found in nematic structures  
 570 at high density conditions. This result is likely due to the excluded volume effect, which limits the  
 571 number of possible platelet states. Accordingly, the macroscopic particle structure significantly  
 572 influenced the pore characteristics, particularly the tortuosity which directly relates to the diffusional  
 573 transport. As mentioned above, the present analysis was performed only for low to moderate density  
 574 conditions. Although the results shown here do not cover all of the dry densities of clays  
 575 generally considered, they capture the discontinuous changes in tortuosity (diffusion coefficient) that  
 576 occur at moderate density conditions. This could be a possible scenario explaining the complicated

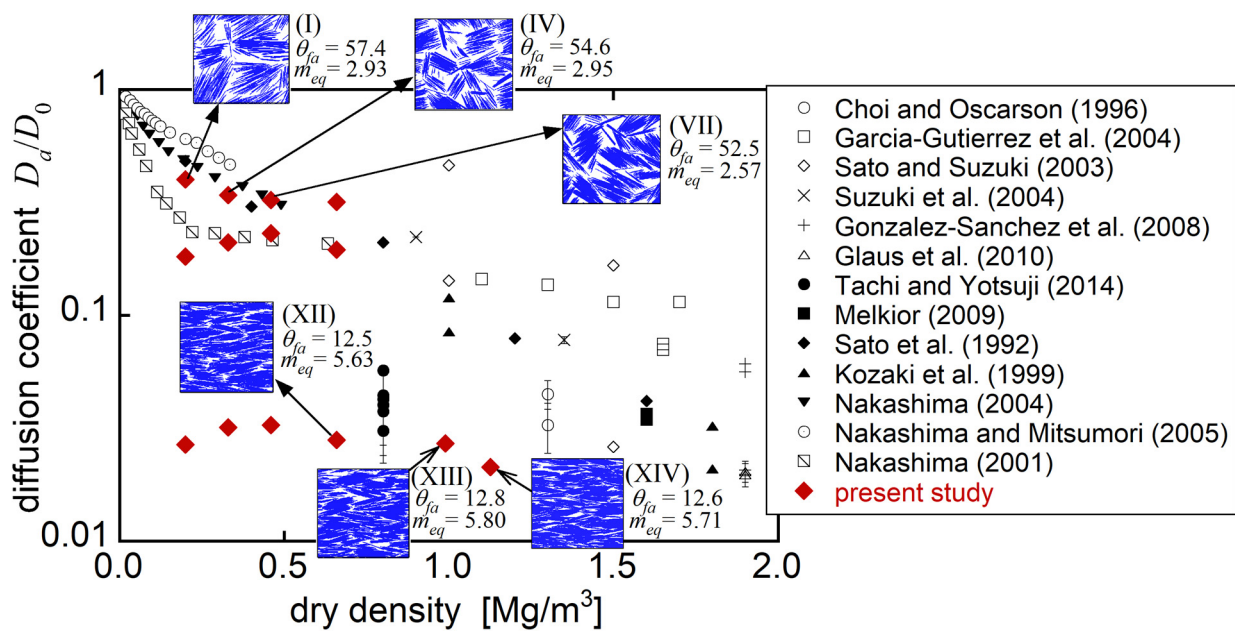


Fig. 8 Comparison of diffusion coefficients from random walk analysis and previous diffusion experiments in smectite type clays.

577

578 diffusivity in clay layers.

579

#### 580 **4. Conclusion**

581 For fundamental understanding of pore characteristics in clay layers composed of  
582 montmorillonite particles, the relationship between the tortuosity which represents the sinuosity and  
583 complexity of pores and macroscopic structures of platelet particles was examined. Monte Carlo  
584 analyses of platelet structures were performed using various initial configurations to investigate how  
585 macroscopic particle structures influence pore networks. Various metastable platelet structures  
586 containing particle clusters were computed for low to moderate density conditions. The pore  
587 characteristics were examined by extracting only those macropores that would contribute to mass  
588 transport.

589 A random walk analysis was also performed on the macropores to estimate the diffusional  
590 tortuosity in the platelet compaction direction. The results indicate that the structural characteristics  
591 of particles, such as the size and angle of platelet clusters, significantly influence the tortuosity. These  
592 results suggest that pore networks in platelet structures may vary depending on the internal  
593 configuration. Therefore, it is important to fully characterize the macroscopic structure of particles  
594 when evaluating mass transport properties such as permeability and diffusion.

595 The effective porosity, orientation angles, and aspect ratios of particle clusters were quantitatively  
596 estimated for each platelet structure. The diffusional tortuosity obtained from random walk analyses  
597 was compared with an existing geometrical tortuosity model. The results indicate a general agreement  
598 between the previous model and the present analysis under specific density conditions, supporting  
599 the validity of the model. This finding indicates a correspondence between diffusional and  
600 geometrical tortuosities, which are differently defined. Based on these results, the macroscopic  
601 structural characteristics are essential parameters for evaluation of tortuosity in platelet structures.

602 The obtained tortuosity from random walk analyses was converted into the diffusion coefficient  
603 and compared with those of previous diffusion experiments in clay layers. Good agreement was

604 observed between the analytical and experimental results at structures with specific aspect ratio and  
605 orientation angle of clusters for low to moderate density conditions. The structural consistency differs  
606 depending on the density condition, indicating that complex diffusivity in clay layers may result from  
607 the diversity of particle structures.

608

## 609 **Acknowledgements**

610 This study was carried out under a contract with the Ministry of Economy, Trade and Industry (METI)  
611 as part of its R&D supporting program titled “Advanced technology development for geological  
612 disposal of TRU waste (FY2020) (JPJ007597)”. We would like to thank Dr. H. Satoh and I. Kobayashi  
613 for many helpful comments and valuable discussions.

614

## 615 **References**

616

- Patil, S. B. and Chore, H. S., Contaminant transport through porous media: An overview of experimental and numerical studies, *Adv. Environ. Res.*, **3**-1 (2014), 45-69.
- Åkesson, M., Kristensson, O., Börgesson, L. and Dueck, A., THM modelling of buffer, backfill and other system components, SKB TR, **10**-44 (2010).
- Carman, P. C., Fluid flow through granular beds, *Trans. Inst. Chem. Eng.*, **15** (1937), 150-156.
- Holzer, L., Wiedenmann, D., Münch, B., Keller, L., Prestat, M., Gasser, P., Robertson, I. and Grobéty, B., The influence of constrictivity on the effective transport properties of porous layers in electrolysis and fuel cells, *J. Mater. Sci.*, **48** (2013), 2934-2952.
- Keller, L. M., Hilger, A. and Manke, I., Impact of sand content on solute diffusion in Opalinus Clay, *Appl. Clay Sci.*, **112-113** (2015), 134-142.
- Clennell, M. B., Tortuosity: a guide through the maze. *Geol. Soc. Lond., Spec. Publ.*, **122** (1997), 299–344.
- Ghanbarian, B., Hunt, A. G., Ewing, R. P. and Sahimi, M., Tortuosity in porous media: A critical review, *Soil. Sci. Soc. Am. J.*, **20** (2013), 1461-1477.
- Fu, J., Thomas, H.R. and Li, C., Tortuosity of porous media: Image analysis and physical simulation, *Earth Sci. Rev.*, **212** (2021), 103439, 1-30.
- Millington, R. J., Gas diffusion in porous media, *Sci.*, **130** (1959), 100-102
- Weissberg, H. L., Effective diffusion coefficient in porous media, *J. Appl. Phys.*, **34** (1963), 2636-2639.
- Boudreau, B. P., The diffusive tortuosity of fine-grained unlithified sediments, *Geochim. Cosmochim. Acta.*, **60** (1996), 3139-3142.
- Koponen, A., Kataja, M. and Timonen, J., Tortuous flow in porous media, *Phys. Rev. E*, **54** (1996), 406-410.
- Ahmadi, M. M., Mohammadi, S. and Hayati, A. N., Analytical derivation of tortuosity and permeability of monosized spheres: A volume averaging approach, *Phys. Rev. E*, **83** (2011), 026312, 1-8.
- Daigle, H. and Dugan, B., Permeability anisotropy and fabric development: A mechanistic explanation, *Water Resour. Res.*, **47** (2011), W12517.



- Dijkstra, M., Hansen, J.-P. and Madden, P. A., Statistical model for the structural and gelation of smectite clay suspensions, *Phys. Rev. E*, **55** (1996), 3044-3053.
- Keller, L. M., Holzer, L., Wepf, R. and Gasser, P., 3D geometry and topology of pore pathways in Opalinus clay: Implications for mass transport, *Appl. Clay Sci.*, **52** (2011), 85-95.
- Wong, R. C. K. and Wang, E. Z., Three-dimensional anisotropic swelling model for clay shale- A fabric approach, *Int. J. Rock Mech. Min. Sci.*, **34** (1997), 187-198.
- Olsen, H. W., Hydraulic flow through saturated clays, *Clays Clay Miner.*, **9** (1960), 131-161.
- Hong, B., Li, X., Wang, L., Wang, L., Xue, Q. and Meng, J., Using the effective void ratio and specific surface area in the Kozeny-Carman equation to predict the hydraulic conductivity of Loess, *Water*, **12**-24 (2020), W12010024.
- Bacle, P., Dufrêche, J.-F., Rotenberg, B., Bourg, I. C. and Marry, V., Modeling the transport of water and ionic tracers in a micrometric clay sample, *Appl. Clay Sci.*, **123** (2016), 18-28.
- Boğan, A., Rotenberg, B., Marry, V., Turq, P. and Noetinger, B., Hydrodynamics in clay nanopores, *J. Phys. Chem. C*, **115** (2011), 16109-16115.
- Li, B., Wong, R. C. K. and Heidari, S., A modified Kozeny-Carman model for estimating anisotropic permeability of soft mudrocks, *Mar. Pet. Geol.*, **98** (2018), 356-368.
- Adams, A. L., Germaine, J. T., Flemings, P. B. and Day-Stirrat, R. J., Stress induced permeability anisotropy of resedimented Boston Blue clay, *Water Resour. Res.*, **49** (2013), 6561-6571.
- Terada, K., Tani, A., Harada, S., Satoh, H. and Hayashi, D., Monte Carlo analysis of montmorillonite particle structures and modeling of dissolution rate reduction, *Mat. Res. Express*, **6** (2018), 035514
- Singh, P. N. and Wallender, W. W., Effects of adsorbed water layer in predicting saturated hydraulic conductivity for clays with Kozeny-Carman equation, *J. Geotech. Geoenviron. Eng.*, **134**-6 (2008), 829-836.
- Satterfield, C. N. and Sherwood, T.K., *The role of diffusion in catalysis*, (1963), Addison-Wesley, Reading, MA.
- Tye, F.L., Tortuosity, *J. Power Sources*, **9** (1983), 89-100.
- Adler, P. M., *Porous media: Geometry and transports*, (1992), Butterworth-Heinemann, Stoneham, MA.
- Vervoort, R.W. and S.R. Cattle, Linking hydraulic conductivity and tortuosity parameters to pore space geometry and pore-size distribution, *J. Hydrol.*, **272** (2003), 36-49.
- García-Gutiérrez, M., Cormenzana, J. L., Missana, T. and Mingarro, M., Diffusion coefficients and accessible porosity for HTO and <sup>36</sup>Cl in compacted FEBEX bentonite, *Appl. Clay Sci.*, **26** (2004), 65-73.
- Gautam, R., Anisotropy in deformations and hydraulic properties of Colorado shale. PhD thesis, Department of Civil Engineering, University of Calgary, (2004).
- Chalindar, S., Charlier, R., Collin, F., Dizier, A., François, B., Fokkens, J., Garitte, B., Gens, A., Chen, G., Hart, J., Laloui, L. and Sillen, X., Thermal impact on the damaged zone around a radioactive waste disposal in clay host rocks, deliverable 13: In situ heating test ATLAS in Mol, *TIMODAZ project. EUROPEAN COMMISSION*, (2010).
- Schneider, J., Flemings, P.B., Day-Stirrat, R.J. and Germaine, J.T., Insights into porescale controls on mudstone permeability through resedimentation experiments, *Geology*, **39** (2011), 1011-1014.
- Wouterse, A., Williams, S. R. and Philipse, A. P., Effect of particle shape on the density and microstructure of random packings, *J. Phys.: Condens. Matter*, **19** (2007), 406215.
- Pusch, R., Stability of bentonite gels in crystalline rock – Physical aspects, SKBF/KBS Technical Report, **84**-04 (1983).
- Choi, J.-W. and Oscarson, D. W., Diffusive transport through compacted Na- and Ca-bentonite, *J. Contam. Hydrol.*, **22** (1996), 189-202.
- Sato, H. and Suzuki, S., Fundamental study on the effect of an orientation of clay particles on diffusion pathway in compacted bentonite, *Appl. Clay Sci.*, **23** (2003), 51-60.
- Suzuki, S., Sato, H., Ishidera, T. and Fujii, N., Study on anisotropy of effective diffusion

coefficient and activation energy for deuterated water in compacted sodium bentonite, *J. Contam. Hydrol.*, **68** (2004), 23-37.

González-Sánchez, F., Van Loon, L. R., Gimmi, T., Jakob, A., Glaus, M. A. and Diamond, L. W., Self-diffusion of water and its dependence on temperature and ionic strength in highly compacted montmorillonite, illite and kaolinite, *Appl. Geochemistry*, **23** (2008), 3840-3851.

Glaus, M. A., Frick, S., Rossé, R. and Van Loon, L. R., Comparative study of tracer diffusion of HTO,  $^{22}\text{Na}^+$  and  $^{36}\text{Cl}^-$  in compacted kaolinite, illite and montmorillonite, *Geochim. Cosmochim. Acta.*, **74** (2010), 1999-2010.

Tachi, Y. and Yotsuji, K., Diffusion and sorption of  $\text{Cs}^+$ ,  $\text{Na}^+$ ,  $\text{I}^-$  and HTO in compacted sodium montmorillonite as a function of porewater salinity: Integrated sorption and diffusion model, *Geochim. Cosmochim. Acta.*, **132** (2014), 75-93.

Melkior, T., Gaucher, E. C., Brouard, C., Yahiaoui, S., Thoby, D., Clinard, C., Ferrage, E., Guyonnet, D., Tournassat, C. and Coelho, D.,  $\text{Na}^+$  and HTO diffusion in compacted bentonite: Effective surface chemistry and related texture, *J. Hydrol.*, **370** (2009), 9-20.

Sato, H., Ashida, T., Kohara, Y., Yui, M. and Sasaki, N., Effect of dry density of some radionuclides in compacted sodium bentonite, *J. Nucl. Sci. Technol.*, **29-9** (1992), 873-882.

Kozaki, T., Sato, Y., Nakajima, M., Kato, H., Sato, S. and Ohashi, H., Effect of particle size on the diffusion behavior of some radionuclides in compacted bentonite, *J. Nucl. Mater.*, **270** (1999), 265-272.

Nakashima, Y., Nuclear magnetic resonance properties of water rich gels of Kunigel-V1 bentonite, *J. Nucl. Sci. Technol.*, **41-10** (2004), 981-992.

Nakashima, Y. and Mitsumori, F.,  $\text{H}_2\text{O}$  self-diffusion restricted by clay platelets with immobilized bound  $\text{H}_2\text{O}$  layers: PGSE NMR study of water-rich saponite gels, *Appl. Clay Sci.*, **28** (2005), 209-221.

Nakashima, Y., Pulsed field gradient proton NMR study of the self-diffusion of  $\text{H}_2\text{O}$  in montmorillonite gel: Effects of temperature and water fraction, *Am. Mineral.*, **85** (2001), 132-138.